# J2.5  ON THE POLARIMETRIC CHARACTERISTICS OF CELLULAR CONVECTION

# IN THE MARINE ATMOSPHERIC BOUNDARY LAYER

Haiyan Li[1,2], William Perrie[1*], Lanli Guo[1]

1. Fisheries and Oceans Canada, Bedford Institute of Oceanography, Dartmouth, Nova Scotia, Canada

2. Graduate University of Chinese Academic of Sciences, Beijing, China

**Abstract:**  Convection in the marine atmospheric boundary layer (MABL) is an important atmospheric phenomenon. As previous studies were limited to single polarization data, their focus was on the variation of intensity of the return radar wave, which was constrained by the existence of a single polarization image pattern. In this paper, we study the polarimetric characteristics of MABL convection using high-resolution data from fully polarimetric RADARSAT-2 synthetic aperture radar (SAR) images. To identify the MABL signature for cellular convection in SAR images, we also use mesoscale atmospheric model simulations that are close in time and spatially collocated with the remote sensing data. We show that the polarimetric characteristics are helpful to distinguish the cellular convection phenomena from wind waves and other processes in the SAR image.

## 1. Introduction

Convection over the ocean constitutes one family of the collection of possible coherent structures that occur in the marine atmospheric boundary layer (MABL). It is important to forecast and parameterize these effects, and to discover the structure and dynamics of these phenomena (Young et al., 2002).

SAR is a powerful sensor to study the vast array of ocean surface phenomena that can inhabit the MABL. Because these phenomena can modulate the local wind stress vector field and change the surface wave spectra on scales comparable to the SAR wavelength, MABL convection can produce characteristic signatures in the radar imagery (Sikora and Ufermann, 2004).

Many observations and studies relate the mottled appearance that often occurs in SAR images with convection processes in the MABL, which helps us understand, forecast and parameterize the structure and dynamics of these phenomena. However, previous studies were limited in that they are based on single polarization data and they focused on the variation of the return radar wave intensity. Thus, until now, development of an understanding of the SAR imaging of

convective processes was hampered, because similar image patterns could result from many possible different oceanic and atmospheric phenomena, such as rain-related convection (Atlas, 1999), upper ocean or surface ocean convection (Romeiser et al, 2004), or surfactants, as may occur in an oil spill. It is necessary to distinguish the various phenomena from one another before we can synthesize the results of observations, theory, and modeling studies, in order to achieve a fuller understanding of their structure and dynamics. In this paper, we focus on the polarimetric characteristics of MABL convection using RADARSAT-2 (hereafter, RS-2) fully polarimetric SAR (hereafter, PolSAR) data.

PolSAR remote sensing measurements potentially yield more useful information than singly polarimetric RS-1 data. In the former case, the parameters entropy ($H$), anisotropy ($A$), average alpha ($\alpha$), from Cloude and Pottier decomposition (1997) can be used as a basis for the development of new classification methods, in the analysis of polarimetric data (Lee et al., 1999; Ferro-Famil et al., 2001; Touzi et al., 2004; Lee and Pottier, 2009). Polarimetric methods have only recently been applied to ocean backscatter data (Schuler et al., 2003., Li et al (2008a,b)., Migliaccio et al (2009)). We are motivated to focus on a polarimetric analysis of MABL convection using high resolution RS-2 PolSAR data, to distinguish atmosphere phenomena from other processes. The intensity of the return wave of HH and VV data, co-polarization phase difference $\phi_{HH-VV}$, entropy $H$, average $\alpha$ and anisotropy $A$ are analyzed in order to investigate and interpret SAR images.

The remainder of the paper is organized as follows. The data are presented in section 2, giving a description of the meteorological conditions. Section 3 presents the WRF model's simulation of the large scale atmospheric phenomena, as well as the small scale details associated with the SAR image; we will show that the WRF simulation verifies that the phenomena in the SAR image is cellular convection. The SAR polarimetric parameters used in the interpretation of the processes in the SAR image are given in section 4, and conclusions, in section 5.

## 2. Data description

In addition to the RS-2 PolSAR data, ocean surface data was obtained from NDBC buoy data

---

\* *Corresponding author address:* William Perrie, BIO, Dartmouth, NS, B2Y 4A2, Canada, e-mail: William. Perrie@dfo-mpo.gc.ca.

(http://www.ndbc.noaa.gov/), vertical atmospheric temperature profile data and synoptic information from North American Regional Reanalysis (NARR) data (http://www.emc.ncep.noaa.gov/mmb/_rreanl/, co-located with SAR images. These data were combined to assess near surface meteorology. NARR data are also used as the initial and boundary data for WRF model simulations. To supplement these data, we also analyzed SSM/I data (http://www.ssmi.com/ssmi/ssmi__description.html) and QuikSCAT L3 data with resolution of 0.25° (http://podaac.jpl.nasa.gov/DATA__ATALOG/quikscatinfo.html) to get additional information on the rain rate and wind field.

## 2.1 PolSAR data

The span of the PolSAR image is shown in Figure 1. The signals are unique among ocean SAR images in that they are dominated by mottled imagery patterns. Numerous examples of this type of mottled backscatter pattern have been seen in SAR images of the sea surface, linking them to convection in the MABL (Sikora et al., 1995).
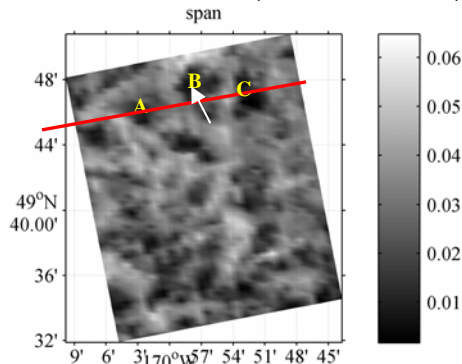


Figure 1. RADARSAT-2 SAR image on 2 February 2009. Interactions with the convective air flow opposite to the ambient wind direction result in a mottled signature which is darker than the background. The transect is used in Figure 6; mottled areas A B C also appear in Figures 5(b), 6 and 7. RADARSAT-2 Data and Products© MacDonald, Dettwiler and Associates Ltd. (2008- 2009) - All Rights Reserved

The RS-2 SAR image was obtained in the North Pacific near the Gulf of Alaska, from the C-band sensor with the single-look full polarization image mode. The sampled pixel spacing was 4.7m over the image domain, 25km × 25km. The imaging time was at UTC 05:05:35 on Feb 2, 2009. The center latitude and longitude coordinates were about 49.8° N and 169.95°W; the center incidence angle was 33.2° and track angle was 11.3°.

## 2.2 Meteorological Conditions

The average fields from 3-hourly NARR data for the pressure-level fields at mean sea level, 500 hPA and 200 hPa (not shown), between UTC 03:00:00 and UTC 06:00:00, on February 2 2009, suggest that the SAR imaging area is located at a ridge of high pressure with a strong low pressure

system developing on the left and a decaying cyclone on the right.

Figure 2 gives the associated 10 m wind field (U10) from QuikSCAT at UTC 06:22:45, on February 2, corresponding to 77 minutes after the SAR imaging time, which indicates that the SAR image is in a low wind regime with wind speeds less than 5m/s. The closest NARR wind field (25 minutes after the SAR image) suggests that U10 is about 2 m/s. The velocity is clearly lower than the case of Young et al (2007) which was in the range 10-12 m/s. NARR data also suggest that the sea surface temperature (SST) and the screen temperature (at 2m height) are about 4.5°C and 0.5°C, respectively. The air-sea temperature difference is about -4°C, suggesting that the atmospheric boundary layer is unstable over the image area. The vertical profiles of temperature (not shown) at UTC 03:00:00 and UTC 06:00:00 indicate that the MABL height (h) is about 850hPa (~ 1250m assuming $\rho_{air}$ =1.2kg/m$^3$).
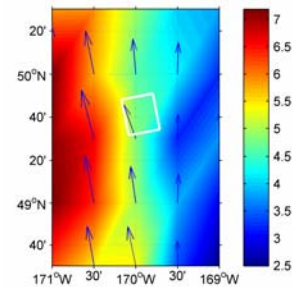


Figure 2. QuikSCAT wind field U10 at UTC 06:22:45, 77 minutes after the SAR image. The white parallelogram indicates the SAR image area.

In a MABL convection roll, the Monin-Obukhov length $L$ is the height at which the turbulent energy generated by buoyancy is more than that generated by wind shear (Stewart, 1985),

$$L \approx \frac{-\left(C_D\right)^{1/2} T_a U_{10}^2}{\kappa g \left(T_s - T_a\right)}$$

(1)

where $CD$ is the drag coefficient with a value about 0.0012, $Ta-Ts$ is the air-sea temperature difference, $Ta$ =273.5K and $Ts$= 277.5K, $U_{10}$ denotes the wind speed at a height of 10 m and the von Karmen's constant $\kappa$ is 0.4. Inserting these values into equation (1), we obtain $L \approx$ -2.3m. Thus the stability parameter of the boundary layer, defined as $h/L$, has the value of -543, the negative sign of the stability parameter suggests that the boundary layer is unstable under 850hPa at the SAR imaging time.

## 2.2 Precipitation

The closest SSM/I data to the SAR image occurred 29 minutes after the SAR image, as presented in Figure 3(a). It shows that the rain rate from F15 SSM/I is almost zero in the SAR scene 29 minutes after SAR imaging time; F15 denotes instruments carried onboard the DMSP series of

polar orbiting satellites. These results are confirmed in Figure 3(b) which gives WRF simulation results suggesting that the integrated precipitation rate is less than 0.25mm over the SAR imaging area (discussed in section 3).
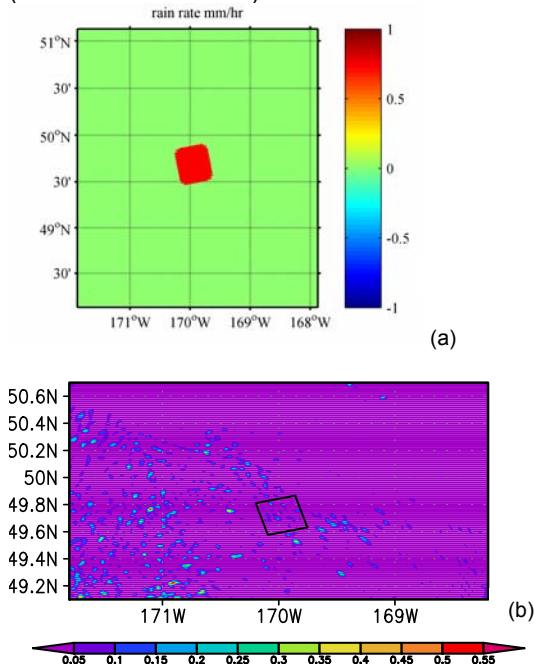


(a)



(b)

Figure 3. Precipitation showing the rain rate from: (a) SSM/I F15 on 2 February 2009, at 29 minutes after the SAR imaging time, and (b) average WRF estimates from UTC 18:00 on 1 February to UTC 05:05 on 2 February 2009. The parallelogram represents the SAR imaging area.

Rainfall is an important factor in the interpretation of SAR images (Alpers and Melsheimer, 2004). The SSM/I data suggests that we can exclude precipitation effects at the moment of SSM/I imaging.

Despite the spatial and temporal offsets of the SSM/I and QuikSCAT data and the coarse resolution of the NARR data relative to the SAR image, they do provide a good overview of the associated meteorological conditions. In addition to temperature and wind measurements, the fact that there probably was no strong precipitation is quite important for interpretation of the SAR image. In principle, heavy rainfall can occur in combination with atmospheric convective cells and can influence the radar signal (Melsheimer et al., 1998). For the scenario studied here, we are confident that this effect can be excluded.

## 3. Atmospheric model simulations

### 3.1 Introduction to the WRF model

We used the WRF3.2 model (Skamarock et al., 2008) to simulate the atmospheric and MABL processes related to the SAR image. WRF was implemented with one-way nested domains

telescoping from 10, 3.33, 1.11Km horizontal grid resolutions, denoted as D1, D2, and D3 in Figure 4. All domains had 31 vertical levels topped at 100 hPa. The outermost D1 covered an area over 42° N – 56° N and 175° E – 155°W, allowing enough space to describe the weather systems over the SAR imaging area, with the inner domains as far away from the model's lateral boundaries as possible. The 3-hourly NARR data were used as the initial and lateral boundary conditions for D1. The simulations start on 29 January at UTC 06:00:00 for D1, and 1 February at UTC 18:00:00 for D2 and D3. They all end at UTC 06:00:00 02 February. We focus on results for the finest grid at 1.11km resolution. The time step for this grid is ~6.7s; model results are output at 5 min intervals.
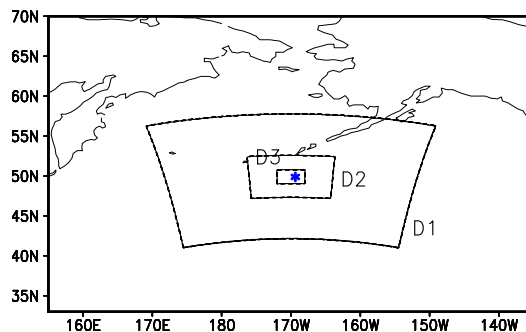


Figure 4 The computation domains for WRF. D1 is the outermost area, D2 is the middle and the D3 is the smallest area. The resolution of D1, D2 and D3 are 10, 3.33, 1.11Km respectively. The SAR image area is indicated by ∗.

### 3.2 WRF model analysis

Both the model results and NARR data show that a cyclone formed at UTC 06:00:00 on 30 Jan 2009 (not shown), with centre at $42^{o}$N, $175^{o}$W, approximately 900 km southwest of the SAR image, and central sea level pressure of 998 hPa.

As the cyclone moved northeastward, the center of the cyclone did not pass through the SAR imaging area but remained always south of this area. The nearest distance between the cyclone center and SAR imaging area is about 200km. The cyclone decayed and moved out the simulation area after 2 February. Moreover, a high pressure ridge gradually formed at the rear of the cyclone and was strengthening over the SAR imaging area, at the time of imaging; at this point the air flow is dominantly in downdraft mode and the atmosphere is stable on the synoptic scale. The advantage of the WRF simulation is that it can describe the small scale processes using the fine-resolution D3 implementation; thus, the cellular convective processes can be identified at the bottom of atmosphere layer, which are lost in NARR's result.

Figure 5 shows the horizontal distribution of the vertical velocity from the WRF simulation. In particular, Figure 5(a) gives the 1000 hPa

distribution of vertical velocity, clearly showing upward and downward air motions with maximal speeds reaching 0.15 m/s and -0.25 m/s, respectively. The upward and downward air flow forms cellular convection at the bottom of the atmosphere. Constrained by stability at the upper portion of the MABL, the convection does not extend above about 850 hPa. The updrafts and downdrafts in the parallelogram shown in Figures 5(a) and 5(b) correspond well with the light and dark areas in the SAR image (Figure 1).
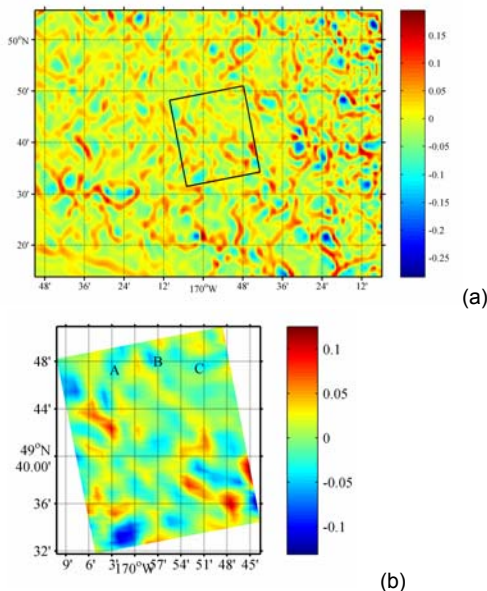


(a)



(b)

Figure 5   The horizontal distribution of vertical velocity field at 1000hPa, and (b), enlargement of parallelogram in (a) representing the SAR imaging area, where A, B and C are indicated in Figure 1.

There are two possible reasons for MABL cellular convection: one is buoyancy, caused by the temperature difference between the ocean surface and MABL air, as suggested by the negative Monin-Obukhov length, and the second is that the synoptic scale air flow is downward, which causes a local upward air floe from the ocean surface, elsewhere in the MABL. The small scale, low level upward and downward air motions form cellular convection. Moreover, the upward and downward air motions interact with the ambient wind field and ocean waves and change the roughness of the ocean surface (Sikora and Ufermann, 2004). Thus, our SAR image appears to have mottled signals.

We use outputs every 5 min from WRF to provide the integrated precipitation from the time period from UTC 18:00:00 on 1 February to the SAR imaging moment at UTC 05:05:35 on 2 February, for the small domain D3. Figure 3(b) suggests that the integrated precipitation rate is less than 0.25mm over the SAR imaging area, indicating that precipitation has almost no effect on the ocean roughness in this area during the 11 hours preceding the SAR imaging time. The WRF

model result supplements the observations by SSM/I data.

WRF results show that the SAR imaging area is influenced by cyclonic activities; after the passage of a vigorous cyclone, a high pressure ridge gradually develops and controls this area. The synoptic scale atmosphere is stable, the precipitation rate is low at the SAR imaging time, and there is almost no precipitation in the preceding 11 hours over the SAR imaging area. However, there clearly are upward and downward air motions at the bottom of atmosphere, which form cellular convection. The mottled signals in the SAR image are cellular convection signatures. In the following discussion, we will analyze the cellular convection signatures in the SAR imagery, as well as the polarimetric characteristics of these phenomena.

## 4.   SAR image

### 4.1 Cellular convection signatures

Cellular convection signatures in SAR intensity images are presented in Figure 1. The scales of cellular convection in the SAR image are mesoscale (Sikora and Ufermann, 2004). The magnitudes of three typical areas, denoted by A, B,C in Figure 1, are about 10km, 10km, 7km in the latitudinal direction, and 6km, 7km, 5km in the longitudinal direction. Radar backscatter increases with wind speed. The highest signal return is obtained looking in an upwind direction. The mean wind direction obtained from the WRF model (not shown) is 18° north to west which is consistent with 20° north to west in the closest (in time) QuikSCAT data (Figures 1 and 3). When the convective air flow is opposite to the ambient wind direction, the resulting mottled signatures are darker than the background signals (indicated by A, B and C), and brighter than the background signal when they are in the same direction as the ambient wind. Thus, brighter and darker signals are present in Figure 1.

### 4.2 Polarimeric characteristics

Fully RS-2 PolSAR data can provide more information than single polarimetric data. Here, we analyze the polarimetric parameters of the cellular convection using high-resolution fully polarized RS-2 data. The polarimetric parameters include the intensity of the return (backscattered) wave for HH and VV, co-polarization phase difference, entropy, average $\alpha$ and anisotropy.   Details about these polarimetric parameters are given by Lee et al. (1999), Ferro-Famil et al. (2001), Li et al. (2008a, b), and Lee and Pottier (2009).

### 4.2.1 Intensity of the return wave

The intensity cross-section is shown in Figure 6. The backscatter intensity of VV polarization is systematically several dB higher than that of the HH polarization. The results are consistent with Melsheiemer and Alpers (1998) and Ufermann and Romeiser (1999). The backscatter intensity for VV

polarization for MABL phenomena is larger than that of oceanic phenomena. The largest modulation depth of area C (Figure 6) is almost 10 dB, which is much larger than results in the range 1–3 dB resulting from theoretical investigations of radar signatures for open-ocean deep convection in favorable conditions (Fischer et al 1999).
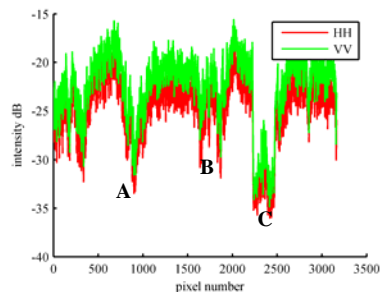


Figure 6. Variations of backscatter intensity cross section on 2 February for HH and VV polarization along the cross-section indicated in Figure 1; A, B and C are in Figure 1.

### 4.2.2 Co-polarization phase differences

Co-polarization phase differences are in the range from 0° to 180°. An ideal single-bounce (or odd-bounce) scatterer will have a co-pol phase difference of 0°, while an ideal double-bounce (or even-bounce) scatterer will have a co-polarizaiton phase difference of 180°. Generally, the ocean surface has low co-polarization phase difference, because the ocean surface is dominated by Bragg-scatter. However, in our case, Figure 7(a) shows that in the cellular convection area, the co-pol phase difference is larger than 60°, especially in area C, and the mean co-pol phase difference reaches 110°, which implies that the dominant scattering mechanism for the ocean surface process is not surface scattering.

### 4.2.3 Polarimetric Entropy

Polarimetric entropy is in the range from 0 to 1, which represents the randomization of the scattering mechanisms. The ocean is regarded as a low-entropy surface dominated by tilted Bragg-scatterers. An exception to this view is discrete (high entropy) wave-breaking events or backscatter at high incidence angle (Morris et al., 2003; Li et al., 2008 b). In the SAR image, there are high entropy areas, as shown in Figure 7 (b). In area C, the mean value is 0.68 and the maximum is 0.76. The entropy of the convection areas experiences a significant increase, indicating that Bragg-scatterers have been reduced by the convective air flow. The interaction between downward air flows and mean wind fields and ocean waves generates more complex, stochastic turbulence, changing the ocean surface roughness and scattering mechanisms.

### 4.2.4 Average polarization scattering angle

The average $\alpha$ angle indicates the dominant type of scattering mechanism. The value has a range that is from 0° to 90°. For $\alpha$ values below 40°,

single bounce surface scatter dominates, whereas for values in the range from 40° to 50°, dipole scatter dominates, and in the range from 50° to 90°, even-bounce scatter dominates. Figure 7(c) gives the polarization scattering angles. The high polarimetric scatter angle indicates that the scattering mechanism in the convection area is not due to the single bounce mechanism as typically observed for the ocean surface. In area C, the mean polarimetric scattering angles reach $60^{\circ}$, implying that the dominant scattering mechanisms are even-bounce and dipole scattering.

### 4.2.5 Anisotropy

Anisotropy is important in trying to understand the properties related to SAR ocean backscatter. The anisotropy range is from 0 to 1. The value of anisotropy is sensitive to surface roughness, for roughness less than 0.5 (Schuler et al, 2002, 2004b); higher anisotropy values indicate a smoother surface. However, in our case, Figure 7(d) suggests that the differences in anisotropy between the surrounding ocean surface and the convection area are not as clear as those of other parameters. Areas A, B and C, have low intensity, high co-polarization phase difference, and high entropy. However, only C has low anisotropy and can be distinguished from the ambient background, whereas A and B are almost the same as other areas and have higher anisotropy than C.

### 5. Conclusions

The regularity of occurrence of mottled SAR imagery is linked with the presence of convection in the MABL. In the case studies presented here, we used ancilliary meteorological data to show that the lower (below 850hPa) atmospheric levels are unstable and the precipitation rate is low. Here, high resolution WRF model simulation results confirm that the phenomenon in the SAR imagery is cellular convection with quite low precipitation rate. The simulation indicates that a vigorous cyclone had passed, and there were upward and downward air flows at the bottom of the atmosphere. The downdrafts and updrafts interact with the ambient wind field and ocean waves and are imaged on SAR. With advanced RS-2 full PolSAR data, we analyzed the polarimetric characteristics of the MABL cellular convection. The intensity of VV polarization is systematically larger than that of HH polarization. Moreover, values for the co-pol phase differences, polarimetric entropy and polarimetric average scatter angles are also much larger than those of wind waves in the open ocean. Anisotropy does not show a consistent variation for convection, unlike the other three polarimetric parameters.The polarimetric parameters do show good potential to distinguish the convection phenomena from ocean surface wind waves.
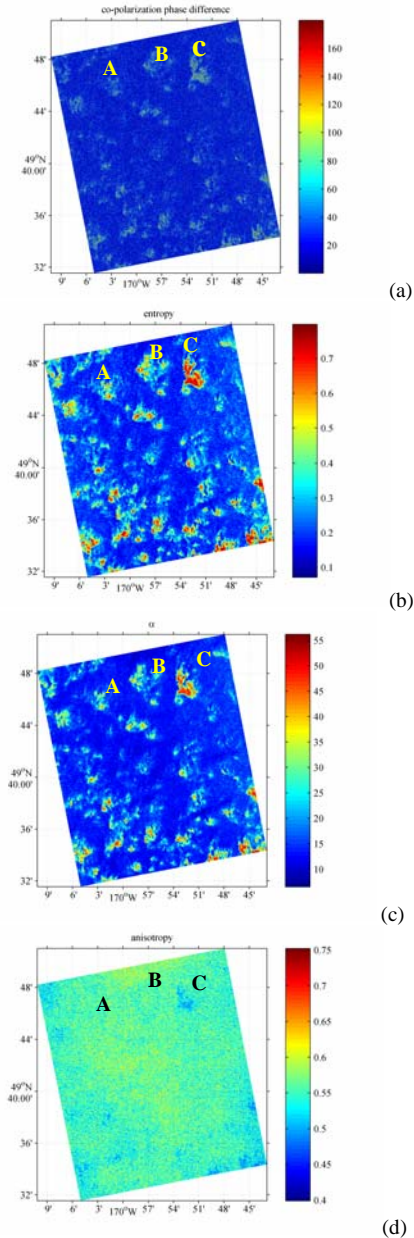
(a)



(b)



(c)



(d)

Figure 7. Analysis of the case on 2 February 2009 for (a) co-polarization phase difference, and (b) entropy, (c) Polarization scattering angle and (d) anisotropy Positions A, B and C are also located in Figure 1.

### References:

Atlas, D., 1994: Footprints of Storms on the Sea: A View from Spaceborne Synthetic Aperture Radar', *J. Geophys. Res.* 99, 7961–7969.

Cloude, S.R., Pottier. E.,1997: Application of the H/A/alpha polarimetric decomposition theorem for land classification, Proceeding of SPIE 1997.

Fischer, K. W., S. Legg, W. H. Munk, R. A. Shuchman, R. W. Garwood, and J. P. Palshook.,1999: Modeled radar surface signature of deep ocean convection, *IEEE Trans. Geosci. Remote Sens.*, 37(4), 2050 – 2067.

Lee, J.S., Grues, M.R., Ainsworth, T.L., Du, L., Schuler, D.L., and Cloude, S.R., 1999: Unsupervised classification of polarimetric SAR images by applying target decomposition and complex Wishart distribution. *IEEE Trans. Geosci. Remote Sens.* 37, (5), 2249–2258.

Lee J. S, Pottier E.,2009: Polarimetric Radar Imaging: From Basics to Applications , Technology & Engineering.

Li, H. Y., He, Y.J, Meng, L., Wang, W.G., 2008 a: Ship detection and characterization with generalized optimization of polarimetric contrast enhancement, *The Chinese Journal of Electronics*, 17(3), 541-545.

Li, H. Y., Zhang, Sh,F., Shen, H., He, Y.J., 2008 b: Polarimetric scatter mechanisms of ocean surface from wave breaking or at large incident angle, Proc. Int. Geoscience and Remote Sensing Symp. (IGARSS), 2008.

Melsheimer, C., Alpers. W., and Gade. M., 1998: Investigation of multifrequency/ multi-polarization radar signatures of rain cells over the ocean using SIR-C/X-SAR data, *J. Geophys. Res.*, 103, 18,867 –18,884.

Migliaccio, M., Nunziata. F., Gambardella. A., 2009: On the co-polarized phase difference for oil spill observation, *International Journal of Remote Sensing*, 30(6) 2009,1587-1602

Romeiser, R., Ufermann, S., Androssov, A., Henning Wehde., Leonid Mitnik., Stefan Kern Angelo Rubino., 2004: On the remote sensing of oceanic and atmospheric convection in the Greenland Sea by synthetic aperture radar, *J. Geophys. Res.*, 109, C03004, doi:10.1029/2003JC001975, 2004

Schuler, D. L., Lee .J.S, Kasilingam D, Nesti G.,2002: Surface Roughness and Slope Measurements Using Polarimetric SAR Data, *IEEE Trans. Geosci. Remote Sens.* 40(3), 687-698.

Schuler, D.L., Kasilingam, D. , Lee, J.-S.,, and Pottier, E., 2003: Studies of ocean wave spectra and surface features using polarimetric SAR, IGARSS'03, Toulouse, France, IEEE, 2003.

Schuler, D.L., Lee, J.-S., G. De Grandi., 2004 b: Spiral Eddy Detection using Surfactant Slick Patterns and Polarimetric SAR Image Decomposition Techniques, Proc. Int. Geoscience and Remote Sensing Symp. IGARSS'2004, 213-215.

Sikora, T. D., Young, G. S.,1995: Use of Spaceborne Synthetic Aperture Radar Imagery of the Sea Surface in Detecting the Presence

and Structure of the Convective Marine Atmospheric Boundary Layer, *Picture of the Month*, 123,3623-3632.

Sikora.T.D.,Ufermann.S., 2004: SAR Marine User's Manual , Chapter 14. Marine Atmospheric Boundary Layer Cellular Convection and Longitudinal Roll Vortices, 321-329. http://www.sarusersmanual.com/

Ufermann, S., and Romeiser, R., 1999, Numerical study on signatures of atmospheric convective cells in radar images of the ocean, *J. Geophys. Res.*, 104, 25,707– 25,720.

Young, G. S., Kristovich, D. S., Hjelmfelt, M. R., and Foster, R. C., 2002: Rolls, Streets,Waves and More: A Review of Quasi-Two Dimensional Structures in the Atmospheric Boundary Layer, *Bull. Amer. Meteorol. Soc.* 83, 997–1001.

Young, G.S., T.D. Sikora, and C.M. Fisher, 2007: Use of MODIS and synthetic aperture radar wind speed imagery to describe the morphology of open cell convection. *Canadian J. of Remote Sens.*, 33, 357-367.

Touzi.R., Boerner.W.M., Lee. J.S., and Lueneburg. E., 2004, A review of polarimetry in the context of synthetic aperture radar: concepts and information extraction, *Can. J. Remote Sensing*, 30, (3): 380–407.